

Bond-order potential for silicon

B. A. Gillespie,¹ X. W. Zhou,² D. A. Murdick,¹ H. N. G. Wadley,¹ R. Drautz,³ and D. G. Pettifor³
¹*Department of Materials Science and Engineering, University of Virginia, Charlottesville, Virginia 22904, USA*
²*Mechanics Materials Department, Sandia National Laboratories, Livermore, California 94550, USA*
³*Department of Materials, University of Oxford, Oxford OX1 3PH, United Kingdom*
 (Received 17 August 2006; revised manuscript received 8 March 2007; published 27 April 2007)

The tight-binding description of covalent bonding is used to propose a four-level, bond-order potential for elemental silicon. The potential addresses both the σ and π bonding and the valence of this sp -valent element. The interatomic potential is parametrized using *ab initio* and experimental data for the diamond cubic, simple cubic, face-centered-cubic, and body-centered-cubic phases of silicon. The bond-order potential for silicon is assessed by comparing the predicted values with other estimates of the cohesive energy, atomic volume, and bulk modulus for the β -Sn, bc8, st12, and 46 clathrate structures. The potential predicts a melting temperature of 1650 ± 50 K in good agreement with the experimental value of 1687 K. The energetics of various high-symmetry point defect structures and the structure and energetics of small silicon clusters are investigated. The potential also provides a robust description of surface reconstructions; it notably predicts with high fidelity the surface formation energy of the (111) 7×7 dimer adatom stacking fault configuration.

DOI: [10.1103/PhysRevB.75.155207](https://doi.org/10.1103/PhysRevB.75.155207)

PACS number(s): 31.15.Qg

I. INTRODUCTION

Because of its great technological importance, silicon is one of the most intensely studied elements in the Periodic Table.¹ Numerous synthesis and processing methods have been developed to enable its use in microelectronic devices.² Deposition tools, such as molecular-beam epitaxy (MBE), enable the growth of very high crystalline quality silicon at deposition rates of $1\text{--}10$ Å/s provided the substrate temperatures are above ~ 450 °C.² This process enables atomic monolayer control of the growth surface to be achieved by manipulating the thermally activated atomic assembly processes. Ion implantation can also be used to create amorphous layers on the surface of silicon which can then undergo epitaxial regrowth at temperatures well below the melting temperature.³ The solid phase epitaxial growth rate is well described by an Arrhenius dependence on temperature (as the temperature increases, the epitaxial growth rate increases), with an experimentally derived activation energy of 2.7 eV for silicon.⁴

There is significant interest in the use of modeling methods to better understand the atomic assembly mechanisms during these vapor phase and solid-state epitaxial growth processes. Numerous computational techniques have been developed to address atomic interaction during atomic structure simulation. Density-functional theory (DFT) calculates the full electronic configuration of a system of atoms using first-principles quantum mechanics. The DFT method is computationally expensive and is typically employed only for small systems (on the order of $10\text{--}100$ atoms).⁵ Kinetic Monte Carlo (KMC) employs a database of known (measured or precomputed) activation barriers for atomic migration and computes jump probabilities between lattice sites to simulate the evolution of a system of atoms. When on-lattice approaches are used, this method is much more computationally efficient than DFT and is capable of simulating systems

containing many millions of atoms.^{6,7} However, the KMC approach requires significant *a priori* knowledge of the diffusion processes, their associated energetics, and surface reaction rates. The compilation of a complete set of this atomic scale information is nontrivial.⁸

Molecular-dynamics (MD) methods lie between the *ab initio* and Monte Carlo approaches in both computational efficiency and predictive validity.⁹ Molecular-dynamics methods solve Newton's equations of motion for atom positions in a system using a potential-energy function (an interatomic potential). They have been successfully used to study the surfaces of transition metals during their assembly from the vapor phase using embedded atom method (EAM) potentials.^{10,11} The approach has also been extended to ion assisted deposition¹² and surfactant mediated growth.¹³ These studies have significantly contributed to the development of modern ion-beam assisted deposition tools for the growth of metallic superlattice structures.¹⁴

Silicon is covalently bonded and more complex to model than the close-packed metals. In contrast to the close-packed phases preferred by metals, silicon has an open diamond cubic structure under ambient equilibrium conditions.¹⁵ Because of sp^3 hybrid bonding, each atom is tetrahedrally coordinated and large energy penalties are incurred by distortions of the lattice. The strong angular dependence of the interaction energy cannot be accounted for by the EAM-type potentials used for close-packed metals. Angularly dependent interatomic potentials are necessary to accommodate the complexity of the covalent bond.

The covalent bonding in silicon arises from electrons in the s and p orbitals.¹⁶ The s orbital is radially symmetric while the three p orbitals are orthogonal to each other. The s and p orbitals can overlap to form σ and π bonds. The σ bond orbitals are symmetric with respect to the bond axis, whereas π bonds are antisymmetric about the same bond axis rotation.¹⁶ Silicon contributes two s and two p electrons to its covalent bonds. In order to maximize the valence electron orbital overlap, the s and p orbitals form four sp^3 hy

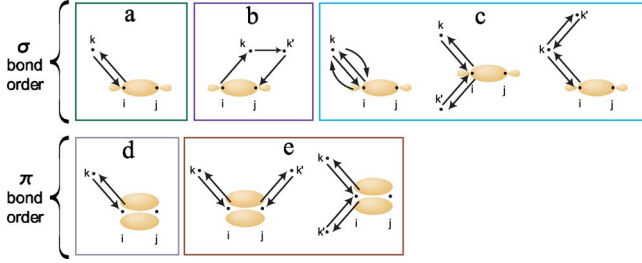


FIG. 1. (Color online) Self-returning [(a), (c), (d), and (e)] and interference (b) hopping paths of lengths 2 and 4 which contribute to (a) $\Phi_{2\sigma}$, (b) $R_{4\sigma}$, (c) $\Phi_{4\sigma}$, (d) $\Phi_{2\pi}$, and (e) $\Phi_{4\pi}$.

brids at the expense of a small energy penalty (the promotion energy). This hybridization is responsible for the tetragonal structure of diamond cubic silicon.¹⁶ The bond order, or strength of the bond, is one-half the difference of the number of bonding electrons and antibonding electrons. It assumes a maximum value of unity for a σ bond and two for a π bond when the bonding orbitals are fully occupied and the antibonding states are empty.

Numerous groups have attempted to incorporate these physical concepts underlying covalent bonding in many-body interatomic potentials.^{17–26} This has led to semiempirical sets of equations that attempt to approximate the phenomenological nature of the bond. An assessment for the GaAs system has shown that this approach has resulted in mixed success.²⁷ Pettifor and co-workers have shown that it is possible to derive an analytic, many-body interatomic potential by coarse graining the electronic structure within the orthogonal two-center tight-binding (TB) representation of covalent bonding.^{28–32} These analytic bond-order potentials (BOPs) explicitly link the bond order (and therefore bond energy) to the positions of atomic neighbors. Applications of the approach to the GaAs system and hydrocarbons have given encouraging results.^{27,33} This paper explores the application of the BOP formalism developed by Pettifor and co-workers to elemental silicon. The resulting interatomic potential is assessed by comparison of its predictions with experimental and *ab initio* data.

II. ANALYTIC BOND-ORDER POTENTIALS

The derivation of the functional format of the BOP from the TB model has been detailed elsewhere.^{28–32} Here, we introduce this format and define the precise form employed for use with the Si elemental system. The potential-energy function (E) is expressed as the sum of bonding U^{bond} , repulsive U^{rep} , and promotion energy U^{prom} terms

$$E = U^{bond} + U^{rep} + U^{prom}, \quad (1)$$

where the bonding energy incorporates elements of both the s and p nature of the covalent bond, the repulsive energy is

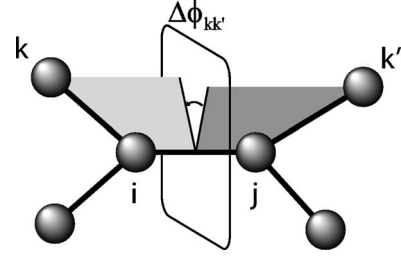


FIG. 2. Dihedral angle formed between atoms $kijk'$.

represented by a pairwise interaction, and the promotion energy represents the energy penalty associated with the orbital hybridization needed to achieve the sp^3 bonding environment.

The bond energy is written as follows:

$$U^{bond} = - \left[\sum_{j=i_1}^{i_N} \beta_{\sigma,ij} \Theta_{\sigma,ij} + \sum_{j=i_1}^{i_N} \beta_{\pi,ij} \Theta_{\pi,ij} \right], \quad (2)$$

where i_1, i_2, \dots, i_N is a list of neighbors of atom i , Θ_{σ} and Θ_{π} are the σ and π bond orders, and β_{σ} and β_{π} are the corresponding bond integrals. The bond-order terms describe the dependence of the ij bond strength on the local configurations. The bond integrals β_{σ} and β_{π} are pairwise functions of the interatomic distance r_{ij} .

$$\beta_{\sigma,ij} = \beta_{\sigma,0} \text{GSP}_{\sigma}(r_{ij}), \quad (3)$$

$$\beta_{\pi,ij} = \beta_{\pi,0} \text{GSP}_{\pi}(r_{ij}), \quad (4)$$

where $\beta_{\sigma,0}$ and $\beta_{\pi,0}$ are constants, and GSP is a Goodwin-Skinner-Pettifor function.³⁴ The pairwise repulsive energy (U^{rep}) is written similarly as

$$U^{rep} = \frac{1}{2} \sum_{j=i_1}^{i_N} \phi_{ij}, \quad (5)$$

$$\phi_{ij} = \phi_0 \text{GSP}_{\phi}(r_{ij}), \quad (6)$$

where ϕ_0 is a constant, and the GSP format takes the form

$$\text{GSP}_x(r_{ij}) = \left(\frac{r_0}{r_{ij}} \right)^{n_x} \exp \left\{ n_x \left[\left(\frac{r_0}{r_{c,x}} \right)^{n_{c,x}} - \left(\frac{r_{ij}}{r_{c,x}} \right)^{n_{c,x}} \right] \right\}, \quad (7)$$

where $x = \phi, \sigma, \pi$ define the function type, and r_0 , r_c , n , and n_c are constants. The GSP function is further modified by application of a cubic function $S(r_{ij})$, so that $\text{GSP}(r_{ij}) \rightarrow \text{GSP}(r_{ij})S(r_{ij})$, to ensure a smooth cutoff of the interaction energy as r_{ij} approaches r_{cut} . This spline is of the form

$$S(r_{ij}) = \begin{cases} 1, & r_{ij} \leq r_1 \\ \left(\frac{r_{ij} - r_{cut}}{r_1 - r_{cut}} \right)^2 \left\{ \frac{3r_1 - 2r_{ij} - r_{cut}}{r_1 - r_{cut}} + n \left(1 - \frac{r_{ij}}{r_1} \right) \left[1 + n_c \left(\frac{r_1}{r_c} \right)^{n_c} \right] \right\}, & r_1 \leq r_{ij} \leq r_{cut} \\ 0, & r_{cut} \leq r_{ij}. \end{cases} \quad (8)$$

The σ bond order (Θ_σ) for the ij bond is given by

$$\Theta_{ij,\sigma} = \left\{ 1 + \frac{\Phi_{2\sigma}^i + \Phi_{2\sigma}^j + \left(\frac{\delta_\sigma}{\beta_{ij,\sigma}}\right)^2 + R_{4\sigma}^{ij} + \tilde{\Phi}_{2\sigma}^i \tilde{\Phi}_{2\sigma}^j (2 + \Delta\tilde{\Phi}_{4\sigma})}{(1 + \Delta\tilde{\Phi}_{4\sigma})^2} \right\}^{-1/2}, \quad (9)$$

where

$$\Delta\tilde{\Phi}_{4\sigma} = \frac{\Delta\Phi_{4\sigma}}{\sqrt{\Delta\Phi_{4\sigma} + \Phi_{2\sigma}^i \Phi_{2\sigma}^j}}, \quad (10)$$

$$\tilde{\Phi}_{2\sigma}^i \tilde{\Phi}_{2\sigma}^j = \frac{\Phi_{2\sigma}^i \Phi_{2\sigma}^j}{\sqrt{\Delta\Phi_{4\sigma} + \Phi_{2\sigma}^i \Phi_{2\sigma}^j}}, \quad (11)$$

and δ_σ is a parameter. The terms $\Phi_{2\sigma}^i$, $\Phi_{4\sigma}^i$, and $R_{4\sigma}^{ij}$ represent the specific self-returning hopping paths illustrated in Fig. 1. They can be written as

$$\Phi_{2\sigma}^i = \sum_{k \neq i,j} g_{jik,\sigma}^2 \left(\frac{\beta_{ik,\sigma}}{\beta_{ij,\sigma}}\right)^2, \quad (12)$$

$$\begin{aligned} \Phi_{4\sigma} = & \sum_{k \neq i,j} g_{jik,\sigma}^2 \left(\frac{\beta_{ik,\sigma}}{\beta_{ij,\sigma}}\right)^4 \\ & + \sum_{k \neq i,j} g_{jik,\sigma} g_{kik',\sigma} g_{k'ij,\sigma} \left(\frac{\beta_{ik,\sigma}}{\beta_{ij,\sigma}}\right)^2 \left(\frac{\beta_{ik',\sigma}}{\beta_{ij,\sigma}}\right)^2 \\ & + \sum_{k,k' \neq i,j} (g_{jik,\sigma} g_{ikk',\sigma})^2 \left(\frac{\beta_{ik,\sigma}}{\beta_{ij,\sigma}}\right)^2 \left(\frac{\beta_{kk',\sigma}}{\beta_{ij,\sigma}}\right)^2, \end{aligned} \quad (13)$$

$$\begin{aligned} R_{ij,4\sigma} = & \sum_{k,k' \neq i,j} g_{jik,\sigma} g_{ikk',\sigma} g_{kk'j,\sigma} g_{ijk',\sigma} \left(\frac{\beta_{ik,\sigma}}{\beta_{ij,\sigma}}\right) \left(\frac{\beta_{kk',\sigma}}{\beta_{ij,\sigma}}\right) \\ & \times \left(\frac{\beta_{k'j,\sigma}}{\beta_{ij,\sigma}}\right), \end{aligned} \quad (14)$$

where

$$\cos[2(\phi_k - \phi_{k'})] = \frac{2(\cos \theta_{kik'} - \cos \theta_{jik'} \cos \theta_{jik})^2 - \sin^2 \theta_{jik} \sin^2 \theta_{jik'}}{\sin^2 \theta_{jik} \sin^2 \theta_{jik'}}, \quad (19)$$

and $\hat{\beta}$ is defined as

$$\hat{\beta}_{ik}^2 = \frac{p}{1+p} \left(\frac{\beta_{ik,\sigma}}{\beta_{ij,\pi}}\right)^2 - \delta \left(\frac{\beta_{ik,\pi}}{\beta_{ij,\pi}}\right)^2, \quad (20)$$

where δ is a constant.

The promotion energy (U^{prom}) can be expressed as

$$g_{jik,\sigma} = 1 + p(\cos \theta_{jik} - 1). \quad (15)$$

Here, p is a parameter. The format of the angular term g has been simplified from the form found in Ref. 32 by assigning a value of 0 to the parameter b_σ .

The π bond order (Θ_π) for the ij bond is given by

$$\Theta_{ij,\pi^\pm} = \left[1 + \frac{\Phi_{2\pi}^i + \Phi_{2\pi}^j \pm \left(\frac{\Phi_{4\pi}^i + \Phi_{4\pi}^j}{2}\right)^{1/2}}{2} \right]^{-1/2}, \quad (16)$$

where the terms $\Phi_{2\pi}$ and $\Phi_{4\pi}$ represent the specific self-returning hopping paths of lengths 2 and 4 illustrated in Figs. 1(d) and 1(e). The parameter c_π found in Ref. 32 for the equivalent π bond-order expression is assigned a value of 1 here. The self-returning hopping paths of lengths 2 and 4 can be written as

$$\Phi_{2\pi}^{ij} = \sum_{k \neq i,j} \left[\sin^2 \theta_{jik} \frac{p}{1+p} \left(\frac{\beta_{ik,\sigma}}{\beta_{ij,\pi}}\right)^2 + (1 + \cos^2 \theta_{jik}) \left(\frac{\beta_{ik,\pi}}{\beta_{ij,\pi}}\right)^2 \right], \quad (17)$$

$$\begin{aligned} \Phi_{4\pi} = & \sum_{k,k' \neq i,j} (\sin^2 \theta_{jik} \sin^2 \theta_{jik'} \hat{\beta}_{ik}^2 \hat{\beta}_{ik'}^2 \\ & + \sin^2 \theta_{jik} \sin^2 \theta_{ijk'} \hat{\beta}_{ik}^2 \hat{\beta}_{ik'}^2 + \sin^2 \theta_{ijk} \sin^2 \theta_{ijk'} \hat{\beta}_{jk}^2 \hat{\beta}_{jk'}^2 \\ & + \sin^2 \theta_{ijk} \sin^2 \theta_{jik'} \hat{\beta}_{jk}^2 \hat{\beta}_{jk'}^2) \frac{\cos(\phi_k - \phi_{k'})}{4}, \end{aligned} \quad (18)$$

where the dihedral angle $\phi_k - \phi_{k'}$, defined in Fig. 2, can be found from

$$U_i^{prom} = \delta \left\{ 1 - \left[1 + \sum_{j \neq i} \left(A \frac{\beta_{ij,\sigma}}{\delta} \right)^2 \right]^{-1/2} \right\}, \quad (21)$$

where A is a constant.

The preceding equations fully define the fourth moment approximation BOP.²⁸⁻³² In order to use the potential for simulations, 19 parameters must be determined. These include 13 GSP (ϕ_0 , $\beta_{\sigma,0}$, $\beta_{\sigma,0}$, n_ϕ , n_σ , n_π , $n_{c,\phi}$, $n_{c,\sigma}$, $n_{c,\pi}$, $r_{c,\phi}$,

TABLE I. Si BOP parameters.

Function	Parameter	Value	
Angular	p	0.7315	
Bond order	δ_σ	0.53741	
	ϕ_0	1.01155	
	$\beta_{\sigma,0}$	2.22435	
	$\beta_{\pi,0}$	0.19631	
	n_ϕ	8.74294	
	n_σ	2.94459	
	n_π	4.04032	
	$n_{c,\phi}$	2.52315	
	GSP	$n_{c,\sigma}$	6.53303
		$n_{c,\pi}$	29.4822
		$r_{c,\phi}$	14.932
		$r_{c,\sigma}$	11.6751
		$r_{c,\pi}$	2.77118
		r_0	2.349
r_1		3.1	
Promotion	r_{cut}	3.6	
	A	1.85202	
	δ	10.17996	

$r_{c,\sigma}$, $r_{c,\pi}$, and r_0), one angular (p), two promotion energy (A and δ), two cutoff (r_1 and r_{cut}), and one bond-order (δ_σ) parameters. A least-squares fitting algorithm was employed to fit the parameters to a database of experimental and *ab initio* properties of silicon. This database included experimental cohesive energies for a silicon dimer and the diamond cubic (dc) phase,¹⁵ local-density-approximation-density-functional-theory (LDA-DFT) estimates for the energy, and bulk modulus of the simple cubic (sc), face-centered-cubic (fcc), and body-centered-cubic (bcc) phases,^{35,36} and experimentally determined elastic moduli (c_{11} , c_{12} , and c_{44}) for the dc phase.³⁷ Calculations of the (2×1) Si(100) surface reconstruction energy (-0.054 eV/ \AA^2) were also used to help fit the parameters. Table I lists the best-fit values of all the parameters. The bulk material properties predicted by the BOP

are compared with the corresponding experimental data and tight-binding calculations used for fitting in Table II.

III. POTENTIAL EVALUATION

The parametrized Si BOP was assessed by examining predicted properties relevant to the atomic assembly of epitaxial thin films grown from the vapor phase. These include the binding energy and structure of the Si trimer, tetramer, pentamer, and hexamer; atomic volume, cohesive energy, and elastic constants for various solid Si phases; the melting temperature; various Si defect formation energies, and the relative surface free energies for (100), (110), (111), and (113) surface reconstructions in the dc Si crystal.

A. Small clusters

The MBE of silicon thin films generally involves the deposition of silicon monomers.^{38,39} However, with the advent of efficient laser vaporization techniques, the vapor phase deposition of small silicon clusters can also be envisioned.^{40–42} Therefore, reasonable predictions of small silicon cluster energies and structures are important. The structure and bond energies of silicon clusters are heavily reliant on both the angular and radial components of the interatomic potential. Thus, examination of cluster properties is a useful means of testing the BOP. A conjugate gradient method⁴³ was used to calculate the relaxed structure and binding energies for small silicon clusters and the results are summarized in Table III along with the Hartree-Fock (HF) predictions.^{44,45}

Three possible configurations for the Si trimer, the linear chain, the bent chain, and the equilateral triangle, were examined. The BOP Si potential predicted that the equilateral triangle had the lowest energy. Data for the linear chain and equilateral triangle were not available for HF calculations.^{44,45} HF calculations predicted that the bent chain has the minimum energy at an apex angle of $\sim 80^\circ$. The apex angle that minimizes the energy of the bent chain was found to be $\sim 111.6^\circ$ using the BOP, matching the minimum of the angular term, Eq. (15).

TABLE II. Comparison of the BOP fitted bulk properties with reference data compiled from experimental (denoted by †) and tight-binding calculations. c_{44} is relaxed. The BOP predictions are listed first followed by the reference data in parentheses.

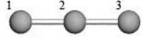
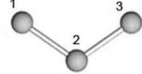
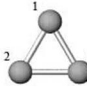

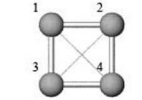
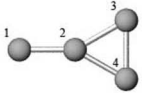
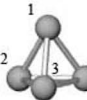
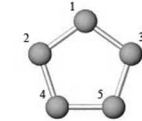
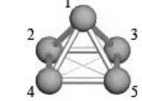
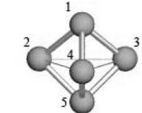
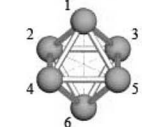
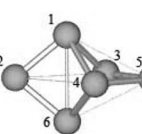
	Dimer	dc	fcc	bcc	sc
E_c (eV/at.)	-2.61 (-2.41 ^{a,†})	-4.63 (-4.63 ^b)	-4.08 (-4.15 ^b)	-4.03 (-4.19 ^b)	-4.43 (-4.29 ^b)
B (GPa)		92.29 (97.88 ^b)	80.95 (93.54 ^b)	74.09 (111.3 ^b)	126.43 (105.6 ^b)
c_{11} (GPa)		134.89 (165.78 ^c)			
c_{12} (GPa)		70.98 (63.94 ^c)			
c_{44} (GPa)		84.03 (79.62 ^c)			

^aReference 15.

^bReferences 35 and 36.

^cReference 37.

TABLE III. Structures, bond lengths, and binding energies predicted for Si_n (n=3–6) small clusters.

	Structure	Point Group	Bond	Bond Length (Å)	Binding Energy (total eV)	
					BOP	HF ^a
trimers		D _{∞h}	1-2	2.37	-4.836	
		C _{2v}	1-2	2.39	-4.645	-3.04
		D _{3h}	1-2	2.47	-4.914	
tetramers		D _{∞h}	1-2 2-3	2.433 2.815	-8.197	-7.29
		D _{4h}	1-2 1-4	2.43 3.437	-8.869	-8.84
		C _{2v}	1-2 2-3 3-4	2.342 2.498 2.487	-7.177	-8.86
		T _d	1-2	2.581	-7.26	-8.09
		D _{5h}	1-2	2.384	-11.611	-10.08
pentamers		C _{4v}	1-2 2-3	2.617 2.50	-11.298	-13.47
		D _{3h}	1-2 1-5 2-3	2.515 3.124 3.415	-11.375	-13.92
		O _h	1-2	2.554	-15.012	
hexamers		C _{2v}	1-2 1-3 2-3 3-4 3-5	2.466 2.506 3.544 3.062 2.466	-15.109	-18.26

^aReferences 44 and 45.

Four Si tetramer structures were examined including the linear chain, the square, the trigonal pyramid, and the corner-capped triangle. The BOP Si potential predicted that the square had the lowest energy. The HF calculations indicated that the square and the capped triangle had the lowest energy (around -8.85 eV). Both the bond length and energy of the square predictions of the BOP agree well with the HF calculations. However, there are some deviations for the other higher-energy structures. For example, the Si_4 linear-chain structure has two separate bond lengths, as shown in Table III. The BOP predicted that the 2-3 bond is significantly (~ 0.4 Å) longer than the 1-2 bond, whereas the HF method predicted that the 2-3 bond is shorter (~ 0.1 Å) than the 1-2 bond. This arises because the BOP overestimates the π -bonding nature in the 1-2 bond.

The BOP predictions for the Si pentamer and hexamer structures are comparable to the HF results. With BOP, the lowest-energy pentamer is the planar pentagon; however, this was not the most stable structure with HF.^{44,45} The planar pentagonal structure favored by the BOP does not provide a significant energetic advantage over the competing high-symmetry cluster structure's predicted energies in BOP predictions. The planar pentagon structure is preferred by BOP due to the minimal amount of bond bending required to obtain the structure (bond angles of 108°). The edge-capped trigonal bipyramid was found by the BOP to be the minimum-energy hexamer structure, in agreement with the HF predictions.^{44,45}

In general, the BOP Si potential prefers larger atomic spacing in clusters than the HF calculations. The source for this discrepancy arises from the selection of the target dimer separation in the BOP parametrization (2.336 Å). The HF underestimates the dimer separation at 2.227 Å (~ 0.11 Å shorter than the experiment).¹⁵ Even though the BOP does not predict the same low-energy structures for Si clusters as those predicted by the HF calculation (with the exception of the Si hexamer), the improvement of the predictions of the overall binding energies for different clusters compared to other potentials is anticipated to improve the simulations of vapor deposition simulation.

B. Bulk structures

During vapor deposition, many different bonding configurations can be encountered by atoms and molecules deposited on the surface. Therefore, it is important for a potential to accurately describe a wide variety of crystalline phases. Many crystalline polymorphs of elemental silicon have been observed. These include the dc,¹⁵ the β -Sn structure,⁴⁶ the bc8 structure,⁴⁷ the st12 structure,⁴⁷ and the Si_{46} clathrate structure.⁴⁸ These phases, along with additional model crystal structures such as sc, fcc, and bcc, were examined. Figure 3 compares the BOP predictions of atomic volume, cohesive energy, and bulk modulus for different phases to those of our LDA-DFT calculations using the VASP calculation package.^{49–52} Note that the LDA-DFT values presented are not the same values to which the potential was fitted. To compare only the energy difference between different phases, the energies were shifted so that the energies pre-

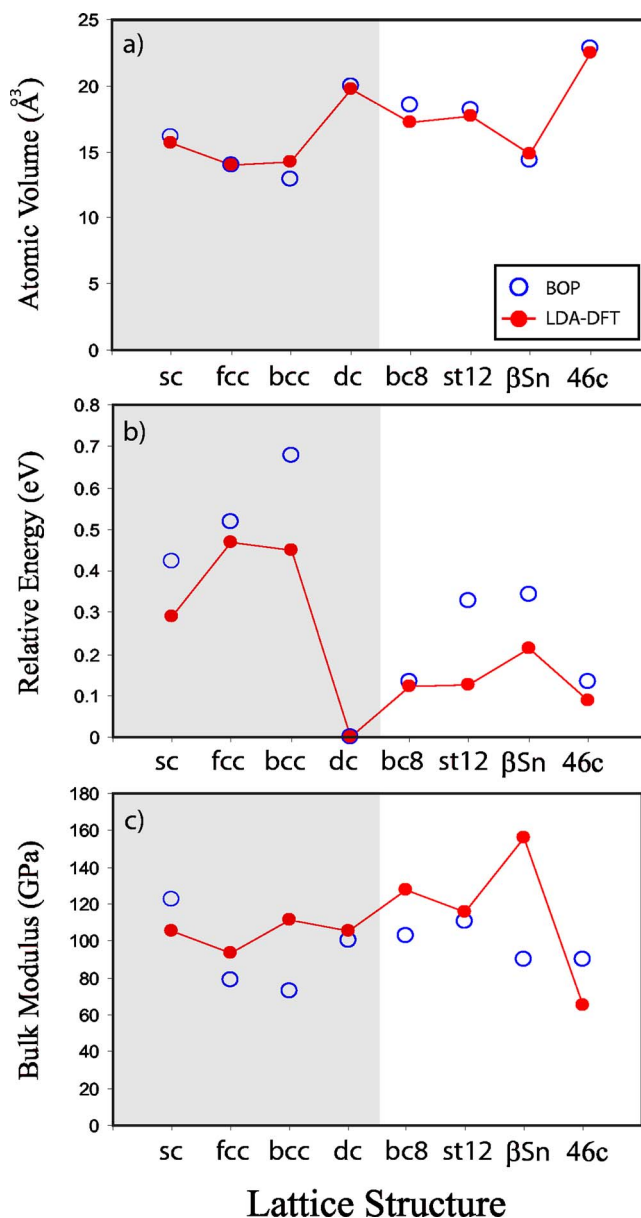


FIG. 3. (Color online) (a) Atomic volume, (b) cohesive energy, and (c) bulk modulus for a variety of physical and theoretical structures as calculated by BOP and LDA-DFT. The values in the shaded region represent fitted values.

dicted by the BOP and LDA-DFT for the diamond cubic phase exactly matched.

The atomic volumes, cohesive energies, and bulk moduli of crystalline structures predicted by the BOP Si potential are in reasonable agreement with the LDA-DFT calculations performed. The atomic volumes predicted by the BOP shown in Fig. 3(a) are within $\pm 3\%$ of the LDA-DFT results, with the exception of the bcc and bc8 structures (both within $\pm 8\%$). The cohesive energies, summarized in Fig. 4(b), are within $\pm 6\%$ of the LDA-DFT results. The bulk moduli, summarized in Fig. 4(c), are within 50% of the LDA-DFT results. This level of bulk modulus prediction is within the acceptable predictive range limitations found within the TB model from which the BOP is derived.⁵³ The Cauchy pressure

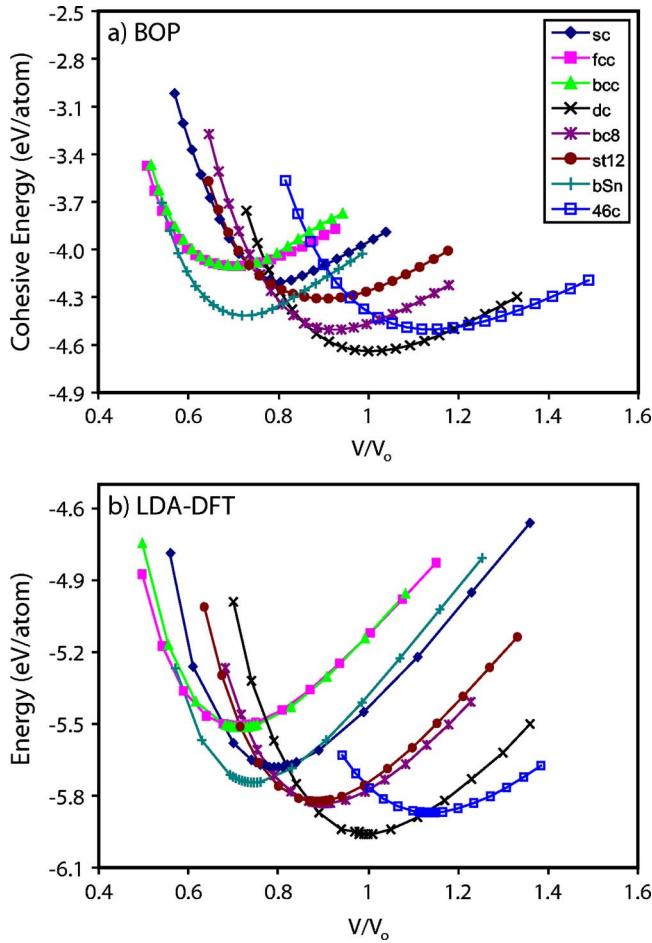


FIG. 4. (Color online) Binding energy vs relative volume (with respect to equilibrium dc volume) curves for a range of Si bulk structures. (a) BOP Si and (b) LDA-DFT.

($c_{12}-c_{44}^{\text{relaxed}}$) was calculated to be -13.05 GPa, in good agreement with the experimental value of -16.0 GPa.⁵⁴ It should be mentioned that interatomic potentials using an environment-independent repulsive term tend to incorrectly predict a positive Cauchy pressure.⁵⁵ The BOP resolves this problem by the incorporation of promotion energy.²⁸⁻³²

At standard temperature and pressure (273 K and 1 atm), the lowest-energy crystalline phase of Si has the diamond cubic structure.¹⁵ The dc structure has an atomic volume of ~ 20 Å³/at. and a cohesive energy of 4.63 eV/at.¹⁵ If sufficient pressure (~ 12.5 GPa) is applied to Si, it will distort from the fourfold coordinated dc structure to a sixfold coordinated β -Sn phase.⁴⁶ This transition is also accompanied by an electronic shift from the semiconducting to metallic state.⁴⁶ When pressure is removed from β -Sn phase silicon, it does not return to the dc phase. Instead, it follows a lower-energy kinetic path to the bc8 phase at a pressure of ~ 8 GPa.⁴⁶ A similar process is required to form the st12 phase; however, increased temperature is necessary when releasing pressure on the β -Sn phase due to a less energetically preferable kinetic pathway for reconfiguring into the st12 structure. The Si₄₆ clathrate structure is obtained through an undescribed set of materials processing involving Na and K.⁴⁸

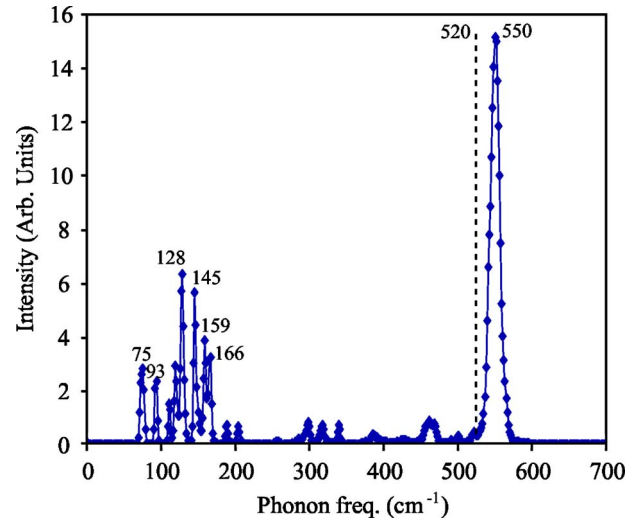


FIG. 5. (Color online) The local phonon spectral density for *c*-Si. The vertical dashed line represents the experimentally observed strongest peak.

To explore the bulk energetics, the binding energy vs atomic volume curves for the structures were examined, and results are shown in Figs. 4(a) and 4(b), respectively, for BOP and LDA-DFT calculations. It is apparent that at a very high pressure, the transition from dc to β -Sn is properly modeled by the BOP. The BOP also correctly places the bc8 phase as a stable phase at an intermediate pressure. The Si₄₆ clathrate structure is also found to be energetically favorable at sufficiently high relative volume (under tensile stresses), matching previous theoretical investigations of the phase.⁴⁸ Comparison between Figs. 4(a) and 4(b) indicates that, in general, the BOP reproduces well the volume-dependent relative energies of different phases of the LDA-DFT calculations.

Examining the bulk phonon spectrum of the diamond cubic phase is also a useful method of evaluating the performance of the potential near equilibrium. This calculation is performed by annealing a sample crystal of sufficient size (512 atoms were employed) and calculating the velocity-velocity autocorrelation function of the system. The vibrational spectrum for the system can then be calculated by taking the Fourier transform of the correlation function. The resulting vibrational spectrum is illustrated in Fig. 5. The highest peak calculated is at 550 cm⁻¹, which is within $\sim 5\%$ of the experimentally observed highest intensity peak at 520 cm⁻¹.⁵⁶

C. Melting temperature

The predicted melting temperature (T_m) can affect surface structures, evaporation rates, and surface diffusion. Near the melting temperature, the interatomic spacing is significantly larger than the separation at room temperature to which the potential has been fitted. Therefore, the melting temperature can be a combinational measure of the strength of the interatomic bond (depth of the interatomic potential well) and the shape of the interatomic potential at large separation. During deposition large interatomic separation distances are fre-

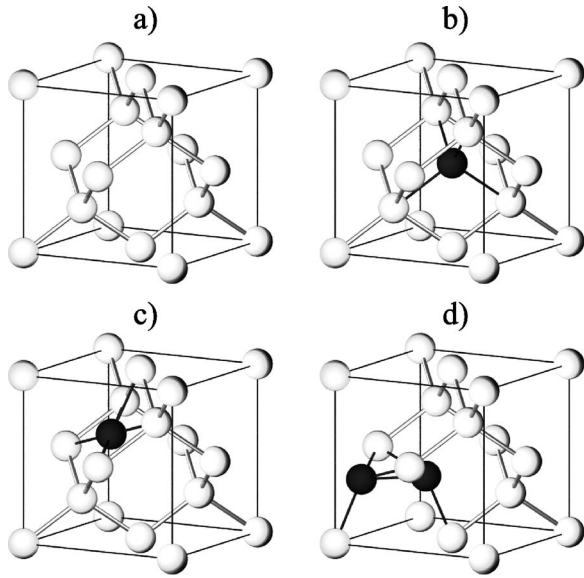


FIG. 6. (a) The diamond cubic lattice and three low-energy interstitial configurations: (b) tetrahedral, (c) hexagonal, and (d) [110]-split.

quently encountered. It is therefore important to examine the melting temperature.

The T_m estimate was determined following the approach by Morris *et al.* in which a half-liquid/half-solid supercell is allowed to achieve an equilibrium temperature under constant pressure.⁵⁷ A large supercell (2160 atoms, 60 plans of 36 atoms each) was used and two temperature control regions were applied, one well above T_m and one well below. After 20 ps, the supercell was $\frac{1}{2}$ melted and $\frac{1}{2}$ crystalline. The temperature control regions were then removed and the system allowed to reach thermal equilibrium (assumed to occur within 500 ps). At equilibrium, the boundary between the liquid and solid phases will have stopped moving, and the temperature of this equilibrated region is taken as the melting temperature. The T_m obtained in this manner has an uncertainty of ± 50 K (obtained from variations in repeated runs).

The BOP silicon potential predicts a melting temperature of 1650 ± 50 K. This temperature range includes the experimentally observed value of $T_m = 1687$ K.⁵⁸ It indicates that the BOP models well the interaction of silicon at large separation distances.

D. Point defects

There is a high probability of defect formation during vapor deposition and solid phase epitaxy. The equilibrium population of the defects is determined by the defect energy. The lifetime of these defects is also determined by kinetics (with the exception of the vacancy); higher temperatures result in significantly lower defect concentration. We have examined several important defects including the three low-energy interstitials and the vacancy.⁵⁹ The interstitial positions and notations are shown in Fig. 6.

The defect formation energy ΔE_f can be expressed following the approach by Finnis⁶⁰ as

TABLE IV. Point defect formation energy in eV.

	BOP	LDA-DFT/ GGA-DFT ^a
T	2.636	3.7–4.8
H	3.846	4.3–5.0
X	3.876	3.3
Vacancy	2.759	3.3–4.3

^aReferences 59 and 61–64.

$$\Delta E_f = \lim_{N \rightarrow \infty} \left\{ E(N, x) - \frac{N_d}{N} E(N, 0) \right\},$$

where $E(N, 0)$ is the total energy of a perfect crystal with N lattice sites, $E(N, x)$ is the total energy of a crystal with N lattice sites and x defects, and N_d is the number of atoms in the defected crystal. The number of lattice sites N used for each sample was 1536, well beyond the point of convergence for this material. The BOP predicted formation energies of the examined point defects are compared to those predicted from LDA-DFT calculations in Table IV.^{59,61–64}

Precise defect formation energies were not expected because defects were not incorporated in the fitting process. As a result, the relative order of the defect energies predicted by the BOP and *ab initio* calculations is not exactly the same. For example, the BOP predicts that the T interstitial has the lowest energy, whereas the LDA-DFT predicts that the X -split interstitial has the lowest energy. Nonetheless, the BOP predicted interstitial energies are generally close to previous LDA-DFT calculations. The vacancy formation energy of 2.759 eV predicted by the BOP also well matches the past GGA-DFT value of 3.17 eV.⁶⁵ The vacancy volume was seen to shrink during energy minimization. This again matches the observations from *ab initio* calculations.⁶⁶

E. Surface reconstructions

A robust description of surface morphology is an important part of the simulation of vapor phase deposition. The most common surfaces that are used for crystal growth in silicon are the (100) and (111) surfaces. The widely observed surface reconstructions for those surfaces are the (2×1) dimer row^{67,68} and the (7×7) dimer adatom stacking fault

TABLE V. Surface energies relative to the corresponding unreconstructed surface. All energies are in eV/Å².

Surface	BOP	<i>Ab initio</i> /TB
(100) (2×1)	−0.046	−0.054 ^a
(110) (2×1) adatom	−0.131	−0.190 ^b
(113) (3×2)	−0.139	−0.036 ^c
(111) (7×7) DAS	−0.379	−0.403 ^d

^aReference 79.

^bReference 73.

^cReferences 74–76.

^dReference 77.

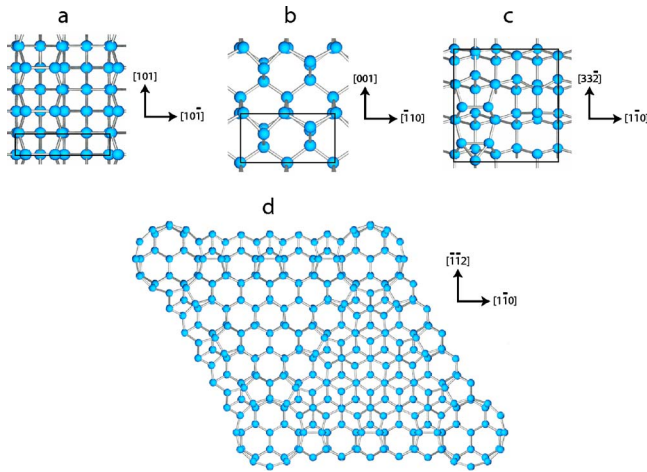


FIG. 7. (Color online) Surface reconstructions for Si. (a) (100) (2×1) adatom, (b) (110) (2×1) adatom, (c) (113) (3×2) DAS, and (d) (111) (7×7) DAS. Unit cells are indicated by a thin solid line box for (a), (b), and (c).

(DAS),⁶⁹ respectively. At low temperatures, the (100) surface is often seen to have a $c(2 \times 4)$ buckled dimer configuration.⁷⁰ It is thought that at higher temperatures, the buckled dimers oscillate at a high frequency such that they appear to be symmetrical.^{68,71,72} The BOP was fitted approximately to the (100) (2×1) surface energy. Here, we examine the (100) (2×1) adatom, the (110) (2×1) adatom,⁷³ the (113) (3×2) DAS,^{74–76} and the (111) (7×7) DAS.⁶⁹ These surfaces are illustrated in Fig. 7. The energies of surfaces were calculated from the surface area, number of atoms, bulk cohesive energy, and total energy of the computational supercell of the reconstructed surface. Each supercell had between 1000 and 2200 atoms with reconstructed top and bottom surfaces. The calculated surface energies relative to the unreconstructed surfaces are compared with the *ab initio*/TB data in Table V.

It can be seen from Table V that the surface free energy relative to the unreconstructed surface is within $0.06 \text{ eV}/\text{\AA}^2$ for each surface except the (113) (3×2) surface. However,

this is not an issue because there is no clear minimum energy reconstruction for the (113) surface in the literature.^{74–76} Most importantly, the highly complex (111) (7×7) surface reconstruction is found to be stable with nearly the same relative free energy as tight-binding calculation.⁷⁷ The BOP shows a marked improvement in the calculation of surface energies over other available silicon interatomic potentials.⁷⁸

IV. CONCLUSIONS

A bond-order potential capable of predicting a range of cluster, bulk, and surface properties for elemental silicon has been developed. Its 19 free parameters were obtained by fitting to experimental and *ab initio* data for the bulk properties of many silicon phases and the surface free energy for the (100) (2×1) reconstruction of the dc surface. The potential has the following characteristics.

(1) The energies and bond lengths, the atomic volume, cohesive energy, bulk modulus of many phases, melting temperature, point defect formation energy, and surface free energy are all relatively well predicted. A negative Cauchy pressure is correctly predicted. The cohesive energy vs atomic volume curves predicted for different phases are in good agreement with LDA-DFT calculations. The predicted vibrational spectrum for silicon also well matches experiment.

(2) Neutral point defect energies predicted by the BOP compare reasonably well with the DFT calculations.

(3) Surface reconstruction free energies were accurately calculated by the Si BOP for the (100), (110), (113), and (111) surfaces, with a notable success for the (111) (7×7) surface energy.

ACKNOWLEDGMENTS

We gratefully acknowledge the support of this work by DARPA and ONR under ONR Contract No. N00014-03-C-0288. C. Schwartz and J. Christodoulou were the program managers.

¹R. Pierret, *Semiconductor Device Fundamentals* (Addison-Wesley, Reading, MA, 1996).

²J. C. Bean, *Growth Techniques and Procedures*, Semiconductors and Semimetals, Vol. 56 (Academic, San Diego, 1999), p. 1.

³G. Lu, E. Nygren, and M. J. Aziz, *J. Appl. Phys.* **70**, 5323 (1991).

⁴E. Ter-Ovanesyan, Y. Manassen, and D. Shachal, *Phys. Rev. B* **50**, 8020 (1994).

⁵B. D. Yu and M. Scheffler, *Phys. Rev. Lett.* **77**, 1095 (1996).

⁶A. B. Bortz, M. H. Kalos, and J. L. Lebowitz, *J. Comput. Phys.* **17**, 10 (1975).

⁷D. T. Gillespie, *J. Comput. Phys.* **22**, 403 (1976).

⁸O. Trushin, A. Karim, A. Kara, and T. S. Rahman, *Phys. Rev. B* **72**, 115401 (2005).

⁹K. Scheersmidt, in *Theory of Defects in Semiconductors 104*,

edited by D. A. Drabold and S. K. Estreicher (Springer, Heidelberg, 2006), pp. 213–244.

¹⁰X. W. Zhou, R. A. Johnson, and H. N. G. Wadley, *Phys. Rev. B* **69**, 144113 (2004).

¹¹X. W. Zhou, H. N. G. Wadley, R. A. Johnson, D. J. Larson, N. Tabat, A. Cerezo, A. K. Petford-Long, G. D. Smith, P. H. Clifton, R. L. Martens, and T. F. Kelly, *Acta Mater.* **49**, 4005 (2001).

¹²X. W. Zhou and H. N. G. Wadley, *J. Appl. Phys.* **87**, 8487 (2000).

¹³W. Zou, H. N. G. Wadley, X. W. Zhou, R. A. Johnson, and D. Brownell, *Phys. Rev. B* **64**, 174418 (2001).

¹⁴H. N. G. Wadley, X. W. Zhou, J. J. Quan, T. Hylton, and D. Baldwin, Non-volatile Memory Technology Symposium, 2003 (unpublished), p. 12-1.

- ¹⁵J. A. Kerr, *CRC Handbook of Chemistry and Physics*, 81st ed., edited by D. R. Lide (CRC, Boca Raton, FL, 2000).
- ¹⁶D. Shriver and P. Atkins, *Inorganic Chemistry*, 3rd ed. (Freeman, New York, 1999).
- ¹⁷F. H. Stillinger and T. A. Weber, *Phys. Rev. B* **31**, 5262 (1985).
- ¹⁸J. Tersoff, *Phys. Rev. Lett.* **56**, 632 (1986).
- ¹⁹J. Tersoff, *Phys. Rev. B* **37**, 6991 (1988).
- ²⁰J. Tersoff, *Phys. Rev. B* **38**, 9902 (1988).
- ²¹X. G. Gong, *Phys. Rev. B* **47**, 2329 (1993).
- ²²A. D. Mistriotis, G. E. Froudakis, P. Vendras, and N. Flytzanis, *Phys. Rev. B* **47**, 10648 (1993).
- ²³B. C. Bolding and H. C. Andersen, *Phys. Rev. B* **41**, 10568 (1990).
- ²⁴D. W. Brenner, *Phys. Rev. B* **42**, 9458 (1990).
- ²⁵K. Ding and H. C. Andersen, *Phys. Rev. B* **34**, 6987 (1986).
- ²⁶D. Conrad and K. Scheersmidt, *Phys. Rev. B* **58**, 4538 (1998).
- ²⁷D. A. Murdick, X. W. Zhou, and H. N. G. Wadley, *Phys. Rev. B* **72**, 205340 (2005).
- ²⁸D. G. Pettifor and I. I. Oleinik, *Phys. Rev. B* **59**, 8487 (1999).
- ²⁹D. G. Pettifor and I. I. Oleinik, *Phys. Rev. Lett.* **84**, 4124 (2000).
- ³⁰D. G. Pettifor and I. I. Oleinik, *Phys. Rev. B* **65**, 172103 (2002).
- ³¹D. G. Pettifor, I. I. Oleinik, D. Nguyen-Manh *et al.*, *Comput. Mater. Sci.* **23**, 33 (2002).
- ³²R. Drautz, X. W. Zhou, D. A. Murdick, B. Gillespie, H. N. G. Wadley, and D. G. Pettifor, *Prog. Mater. Sci.* **52**, 196 (2007).
- ³³M. Mrovec, M. Moseler, C. Elsasser, and P. Gumbsch, *Prog. Mater. Sci.* **52**, 230 (2007).
- ³⁴L. Goodwin, A. J. Skinner, and D. G. Pettifor, *Europhys. Lett.* **9**, 701 (1989).
- ³⁵N. Bernstein, M. J. Mehl, D. A. Papaconstantopoulos, N. I. Papanicolaou, M. Z. Bazant, and E. Kaxiras, *Phys. Rev. B* **62**, 4477 (2000).
- ³⁶N. Bernstein, M. J. Mehl, and D. A. Papaconstantopoulos, *Phys. Rev. B* **66**, 075212 (2002).
- ³⁷G. Simmons and H. Wang, *Single Crystal Elastic Constants and Calculated Aggregate Properties: A Handbook*, 2nd ed. (MIT, Cambridge, MA, 1971).
- ³⁸B. W. Dodson, *Phys. Rev. B* **33**, 7361 (1986).
- ³⁹M. Schneider, I. K. Schuller, and A. Rahman, *Phys. Rev. B* **36**, 1340 (1987).
- ⁴⁰T. G. Dietz, M. A. Duncan, D. E. Powers, and R. E. Smalley, *J. Chem. Phys.* **74**, 6511 (1981).
- ⁴¹M. D. Morse, J. B. Hopkins, P. R. R. Langridge-Smith, and R. E. Smalley, *J. Chem. Phys.* **79**, 5316 (1983).
- ⁴²J. L. Gole, J. H. English, and V. E. Bondybey, *J. Phys. Chem.* **86**, 2560 (1982).
- ⁴³W. H. Press, *Numerical Recipes in Fortran 77: The Art of Scientific Computing*, 2nd ed. (Cambridge University Press, New York, 1996), Vol. 1.
- ⁴⁴K. Raghavachari and V. Logovinsky, *Phys. Rev. Lett.* **55**, 2853 (1985).
- ⁴⁵K. Raghavachari, *J. Chem. Phys.* **84**, 5672 (1986).
- ⁴⁶P. Villars and L. D. Calvert, *Pearson's Handbook of Crystallographic Data for Intermetallic Phases*, 2nd ed. (ASM International, Materials Park, OH, 1991).
- ⁴⁷J. Crain, S. J. Clark, G. J. Ackland, M. C. Payne, V. Milman, P. D. Hatton, and B. J. Reid, *Phys. Rev. B* **49**, 5329 (1994).
- ⁴⁸G. B. Adams, M. O'Keeffe, A. A. Demkov, O. F. Sankey, and Y.-M. Huang, *Phys. Rev. B* **49**, 8048 (1994).
- ⁴⁹G. Kresse and J. Hafner, *Phys. Rev. B* **47**, 558 (1993); **49**, 14251 (1994).
- ⁵⁰G. Kresse and J. Furthmuller, *Comput. Mater. Sci.* **6**, 15 (1996).
- ⁵¹G. Kresse and J. Furthmuller, *Phys. Rev. B* **54**, 11169 (1996).
- ⁵²G. Kresse and J. Hafner, *J. Phys.: Condens. Matter* **6**, 8245 (1994).
- ⁵³D. A. Murdick, X. W. Zhou, H. N. G. Wadley, D. Nguyen-Manh, R. Drautz, and D. G. Pettifor, *Phys. Rev. B* **73**, 045206 (2006).
- ⁵⁴G. Simmons and H. Wang, *Single Crystal Elastic Constants and Calculated Aggregate Properties: A Handbook* (MIT, Cambridge, MA, 1971).
- ⁵⁵M. J. Cawkwell, V. Vitek, D. Nguyen-Manh, and D. G. Pettifor, in *Multiscale Phenomena in Materials—Experiments and Modeling Related to Mechanical Behavior*, MRS Symposia Proceedings No. 779 (Materials Research Society, Pittsburgh, 2003). p. W5.5.
- ⁵⁶J. C. Tsang, K. Eberl, S. Zollner, and S. S. Iyer, *Appl. Phys. Lett.* **61**, 961 (1992).
- ⁵⁷J. R. Morris, C. Z. Wang, K. M. Ho, and C. T. Chan, *Phys. Rev. B* **49**, 3109 (1994).
- ⁵⁸G. W. C. Kaye and T. H. Laby, *Tables of Physical and Chemical Constants*, 15th ed. (Longman, London, UK, 1993).
- ⁵⁹W. Lee, S. Lee, and K. J. Chang, *J. Phys.: Condens. Matter* **10**, 995 (1998).
- ⁶⁰M. Finnis, *Interatomic Forces in Condensed Matter* (Oxford University Press, Oxford, 2003).
- ⁶¹K. C. Pandey, *Phys. Rev. Lett.* **57**, 2287 (1986).
- ⁶²Y. Bar-Yam and J. D. Joannopoulos, *Phys. Rev. Lett.* **52**, 1129 (1984).
- ⁶³P. J. Kelly and R. Car, *Phys. Rev. B* **45**, 6543 (1992).
- ⁶⁴H. Seong and L. J. Lewis, *Phys. Rev. B* **53**, 9791 (1996).
- ⁶⁵S. Goedecker, T. Deutsch, and L. Billard, *Phys. Rev. Lett.* **88**, 235501 (2002).
- ⁶⁶J. L. Mercer, J. S. Nelson, A. F. Wright, and E. B. Stechel, *Modell. Simul. Mater. Sci. Eng.* **6**, 1 (1998).
- ⁶⁷R. E. Schiler and H. E. Farnsworth, *J. Chem. Phys.* **30**, 917 (1959).
- ⁶⁸R. M. Tromp, R. J. Hamers, and J. E. Demuth, *Phys. Rev. Lett.* **55**, 1303 (1985); R. J. Hamers, R. M. Tromp, and J. E. Demuth, *Phys. Rev. B* **34**, 5343 (1986).
- ⁶⁹K. Takayanagi, Y. Tanishiro, M. Takahashi, and S. Takahashi, *J. Vac. Sci. Technol. A* **3**, 1502 (1985).
- ⁷⁰R. A. Wolkow, *Phys. Rev. Lett.* **68**, 2636 (1992).
- ⁷¹J. Dabrowski and M. Scheffler, *Appl. Surf. Sci.* **56**, 15 (1992).
- ⁷²Y. Fukaya and Y. Shigeta, *Phys. Rev. Lett.* **91**, 126103 (2003).
- ⁷³A. A. Stekolnikov, J. Furthmuller, and F. Bechstedt, *Phys. Rev. B* **70**, 045305 (2004).
- ⁷⁴W. Ranke, *Phys. Rev. B* **41**, 5243 (1990).
- ⁷⁵J. Dabrowski, H. J. Mussig, and G. Wolff, *Phys. Rev. Lett.* **73**, 1660 (1994).
- ⁷⁶J. Wang, A. P. Horsfield, D. G. Pettifor, and M. C. Payne, *Phys. Rev. B* **54**, 13744 (1996).
- ⁷⁷G. X. Qian and D. J. Chadi, *Phys. Rev. B* **35**, 1288 (1987).
- ⁷⁸H. Balamane, T. Halicioglu, and W. A. Tiller, *Phys. Rev. B* **46**, 2250 (1992).
- ⁷⁹J. M. Howe, *Interfaces in Materials* (Wiley-Interscience, New York, 1997).